Band-gap formation and morphing in α-T_3 superlattices

S. M. Cunha [1,2,*] D. R. da Costa [2] J. Milton Pereira, Jr.,[2] R. N. Costa Filho [2] B. Van Duppen,[1,†] and F. M. Peeters [1]

[1]*Department of Physics, University of Antwerp, Groenenborgerlaan 171, B-2020 Antwerp, Belgium*
[2]*Departamento de Física, Universidade Federal do Ceará, Campus do Pici, Fortaleza, Ceará, Brazil*

Electrons in α-T_3 lattices behave as condensed-matter analogies of integer-spin Dirac fermions. The three atoms making up the unit cell bestow the energy spectrum with an additional energy band that is completely flat, providing unique electronic properties. The interatomic hopping term, α, is known to strongly affect the electronic spectrum of the two-dimensional (2D) lattice, allowing it to continuously morph from graphenelike responses to the behavior of fermions in a dice lattice. For pristine lattice structures the energy bands are gapless, but small deviations in the atomic equivalence of the three sublattices will introduce gaps in the spectrum. It is unknown how these affect transport and electronic properties such as the energy spectrum of superlattice minibands. Here we investigate the dependency of these properties on the parameter α accounting for different symmetry-breaking terms, and we show how it affects band-gap formation. Furthermore, we find that superlattices can force band gaps to close and shift in energy. Our results demonstrate that α-T_3 superlattices provide a versatile material for 2D band-gap engineering purposes.

I. INTRODUCTION

The isolation of a stable single layer of carbon atoms arranged in a hexagonal lattice, known as graphene [1], combined with the extraordinary electronic and transport properties observed in the atomically thin material [1–4], has motivated many researchers to investigate and produce other two-dimensional (2D) materials [1,5–7]. The peculiar electronic properties of graphene are the result of charge carriers described by an equation analogous to the Dirac one for relativistic particles, but here the presence of a variable similar to a spinor representation, different from the "real" one, results only from the crystal structure instead of from an intrinsic property of the particles. Therefore, the charge carriers in graphene are commonly referenced as pseudospin-1/2 particles [8,9]. These particles have a linear energy dispersion where valence and conduction bands touch each other in special points in reciprocal space called Dirac points [2,3,8,9].

Two-dimensional materials can be subjected to electrostatic potentials with a periodicity significantly larger than the interatomic distance [10–13]. Because one can easily change the strength of the electrostatic potential, this method has been thoroughly investigated as a way to tune electronic properties of the charge carriers in these 2D systems [14–20]. Superlattice potentials are known to increase the number of Dirac points of graphene [16–18,21–25] and as such introduce new physical modes at zero energy, as recently observed in Ref. [26]. Some relevant applications that originated from periodic structures are electron beam supercollimation and electron wave filter [24,25].

Recently, novel and distinctive physics has emerged from 2D systems when adding an additional atom in their crystal structure [27–34], which leads to their charge carriers in a low-energy approach being described as enlarged pseudospin Dirac fermions [31,32,35–37]. Among these systems, we have a Lieb lattice with the additional atom at the edges of a square lattice, which was recently obtained by adding carbon monoxide molecules to a substrate [28], and the T_3 or dice lattice, which has an additional atom at the center of the hexagonal structure. In both, different from graphene, the massless Dirac fermions are described as spin-1 particles and an additional flatband touching the top of the valence and the bottom of the conduction linear bands [38,39]. This flatband has important and unusual effects on the electronic properties due to its dispersionless nature and thus an infinite effective mass [37–45]. Moreover, flatbands are predicted to be important in the search for room-temperature superconductivity [46,47].

The graphene hexagonal lattice and T_3 or dice lattice are incorporated in the α-T_3 model [38,42–45,48]. It allows a tuning between the central atom arrangement and the hexagonal structure by varying the parameter α. Graphene and T_3 are the limiting cases $\alpha = 0$ and 1, respectively.

The α-T_3 model has been useful to investigate physical systems presenting Dirac fermions with a larger pseudospin value. The α-T_3 model was originally proposed to describe the diamagnetic-to-paramagnetic transition in the orbital susceptibility in an optical lattice of cold atoms [49,50]. The limiting case $\alpha = 1$ corresponds to the dice lattice, which can be obtained by stacking three layers of $SrTiO_3/SrIrO_3/SrTiO_3$ [51], or it can be generated by controlling three laser beams propagating in towards a two-dimensional layer of cold atoms [52]. Likewise, this model with appropriate doping and for the case $\alpha = 1/\sqrt{3}$ can be used to describe the three-dimensional $Hg_{1-x}Cd_xTe$ system [53,54].

*sofiacunha@fisica.ufc.br
†ben.vanduppen@uantwerpen.be

Curiously, systems with charge carriers described as spin-1 massless Dirac fermions for certain energy conditions have an angular independent Klein tunneling through rectangular electrostatic barriers, which is called super-Klein tunneling (SKT). This isotropic transmission is unlike single and bilayer graphene, which show highly anisotropic transmission across such barriers. In addition, the tunneling into the flatband across a potential step for a generalized pseudospin has been discussed as well [31,36]. Previous studies considering Dirac fermions across electrostatic potentials in systems with intermediate values of α reveal perfect transmission for normal incidence, and a general trend of enhanced transmission with increasing α [36,45,48]. Moreover, when more barriers are considered, in the case of the dice lattice the tunneling shows little dependence on the number of barriers, whereas for graphene the number of barriers strongly affects the tunneling [55].

Several studies have been published aiming at a way to create a band gap in these structures [44,56–60]. This is necessary for practical electronic applications such as the fabrication of quantum information devices. It was demonstrated that an additional mass term in α-T_3 systems distorts the linear bands around the Dirac cone and produces an energy gap with a third band in it which could be flat or dispersive [43,44]. The position of this band inside the band gap has important consequences for Klein tunneling of massive Dirac fermions across potential barriers.

Motivated by the richness of the tunneling properties and the peculiar electronic properties of Dirac fermions with integer pseudospin, and aiming at understanding how the band gap in α-T_3 systems varies as a function of the tuning parameter α in the presence of superperiodicity, we investigate the energy spectra and density of states (DOS) first in ungapped α-T_3 superlattices, and subsequently we take into account the effect of different symmetry-breaking terms. In both cases, we pay special attention to the appearance of minibands, its band flatness, and its dependence on the coupling parameter α.

This paper is organized as follows. In the second section, we discuss the electronic properties of charge carriers in α-T_3 lattices and how this is affected by small deviations in the atomic equivalence between the sites and the presence of mass terms. In the third section, we develop the transfer-matrix approach to analyze the energy spectra of Dirac fermions in α-T_3 in the presence of a 1D periodic potential. In the fourth section, we discuss the band-gap morphing and its dependence on (i) the coupling parameter and (ii) the symmetry-breaking between the atomic sites by the inclusion of different mass terms. Conclusions are presented in the fifth section.

II. FERMIONS IN α-T_3 LATTICES

A. Energy spectrum and eigenstates

An α-T_3 lattice is formed by the superposition of three triangular sublattices [32]. Two of them are formed by atom sites A and B arranged in a hexagonal lattice with hopping term t. The additional site C is connected only to sites B by a hopping term tuned by a parameter α, which is the parameter that provides a continuous transition from the honeycomb ($\alpha = 0$) to the dice ($\alpha = 1$) lattice and determines the strength
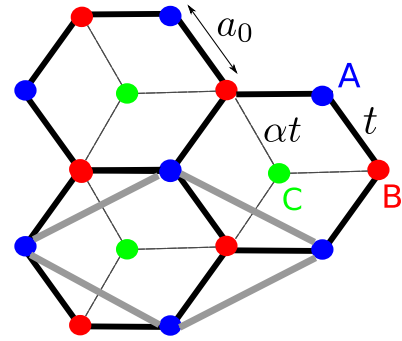

FIG. 1. Schematic of the α-T_3 lattice where the sites of the three sublattices are colored differently. The limit $\alpha = 0$ corresponds to the honeycomb lattice (graphenelike), and $\alpha = 1$ corresponds to the dice lattice. The hopping amplitude between the different atoms is indicated. The region bounded by the gray lines corresponds to the unit cell.

of coupling between the C atoms at the center of the honeycomb lattice, as shown in Fig. 1. The distance between the A, B, and C atoms is the same and is denoted by a_0. The hopping parameters t, α, and a_0 depend on the specific atomic composition of the lattice under consideration and completely determine the properties of the α-T_3 lattice.

The presence of the additional site C centered in the honeycomb lattice results in some interesting electronic properties, such as, e.g., the presence of a flatband in addition to the linear bands and the larger value of pseudospin of charge carriers in these lattices [31,32,38,42,45,51–54].

The lattice structure determines the kinetic energy of the fermions in the material. The low-energy Hamiltonian of fermions in an α-T_3 lattice around the K point is given by the 3×3 matrix expressed in the sublattice basis $|\Psi\rangle = (|\psi_A\rangle, |\psi_B\rangle, |\psi_C\rangle)$ as [32,42]

$$\hat{H}_{\text{kin}} = \begin{pmatrix} 0 & f_\xi(\vec{k})\cos\theta & 0 \\ f_\xi^*(\vec{k})\cos\theta & 0 & f_\xi(\vec{k})\sin\theta \\ 0 & f_\xi^*(\vec{k})\sin\theta & 0 \end{pmatrix}. \quad (1)$$

In Eq. (1) we introduced the parameter $\theta = \tan^{-1}\alpha$, where $\theta = 0$ and $\theta = \pi/4$ correspond to honeycomb and dice lattices, respectively. The function $f_\xi(\vec{k}) = v_F(\xi k_x - ik_y)$, with $v_F = 3a_0 t/2\hbar$ the Fermi velocity and $\vec{k} = (k_x, k_y)$ the wave vector. Here, $\xi = \pm 1$ is the valley index for the K and K' valleys, respectively [32,42]. In the absence of external potentials, the eigenstates of the Hamiltonian are given by

$$|\Psi_\pm\rangle = \begin{pmatrix} \cos\theta\, e^{i\phi_k} \\ \pm 1 \\ \sin\theta\, e^{-i\phi_k} \end{pmatrix}, \quad (2)$$

with eigenvalues $E_\pm = \pm\hbar v_F k$, where $\pm$ indicates the conduction and valence bands, respectively. The angle $\phi_k = \tan^{-1}(k_y/k_x)$ corresponds to the angle associated with the momentum vector. In addition, a flatband state is found,

$$|\Psi_0\rangle = \begin{pmatrix} \cos\theta\, e^{i\phi_k} \\ 0 \\ \sin\theta\, e^{-i\phi_k} \end{pmatrix}, \quad (3)$$
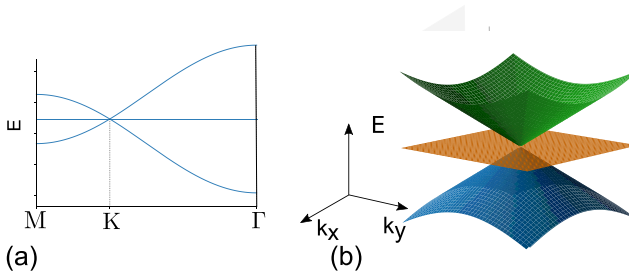
FIG. 2. Energy spectrum of massless Dirac fermions in the α-T_3 lattice (a) in the full first Brillouin zone, and (b) around the K point.

with eigenvalue $E = 0$ corresponding to strongly degenerate states [31,51,52], as represented in Fig. 2. Notice that the energy eigenvalues E do not depend on θ. The parameter is solely affecting the eigenstates.

B. Introduction of a band gap

The Dirac point at $E = 0$ in the pristine α-T_3 lattice is triply degenerate as seen in Fig. 2. This degeneracy is produced by the equivalence of the three sublattices. Breaking this equivalence will lead to a lifting of the degeneracy and the introduction of a band gap. In general, one can include this in the Hamiltonian by a term proportional to $\hat{U}$ that enters as follows:

$$\hat{H} = \hat{H}_{\text{kin}} + \Delta \hat{U}, \tag{4}$$

with $\hat{H}_{\text{kin}}$ given by Eq. (1), and Δ measures the strength of the symmetry breaking. The Hamiltonian in Eq. (4) is obtained from an expansion of the tight-binding model to the nearest neighbors of the α-T_3 lattices around the K point of the first Brillouin zone when different on-site energies are considered [38,42,52]. In this work, we consider two different forms of $\hat{U}$, respectively, given by

$$\hat{U}_1 = \begin{pmatrix} 1 & 0 & 0 \\ 0 & -1 & 0 \\ 0 & 0 & 1 \end{pmatrix}, \quad \hat{U}_2 = \begin{pmatrix} 1 & 0 & 0 \\ 0 & 0 & 0 \\ 0 & 0 & -1 \end{pmatrix}. \tag{5}$$

The effects of the inclusion of the terms $\hat{U}_1$ and $\hat{U}_2$ on the energy spectrum are shown in Figs. 3 and 4, respectively.

The term $\hat{U}_1$ introduces a site energy on the different sublattices, as has been discussed for photonic crystals and optical lattices [56,57]. The solution of $\hat{H} \Psi = E \Psi$ for this case gives
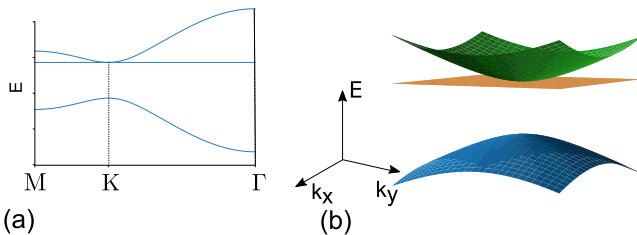

FIG. 3. Energy spectrum of Dirac fermions for arbitrary values of the parameter θ in the α-T_3 lattice when the symmetry-breaking term $\hat{U} = \hat{U}_1$ is used in Eq. (4). (a) Full first Brillouin zone, and (b) spectrum around the K point.
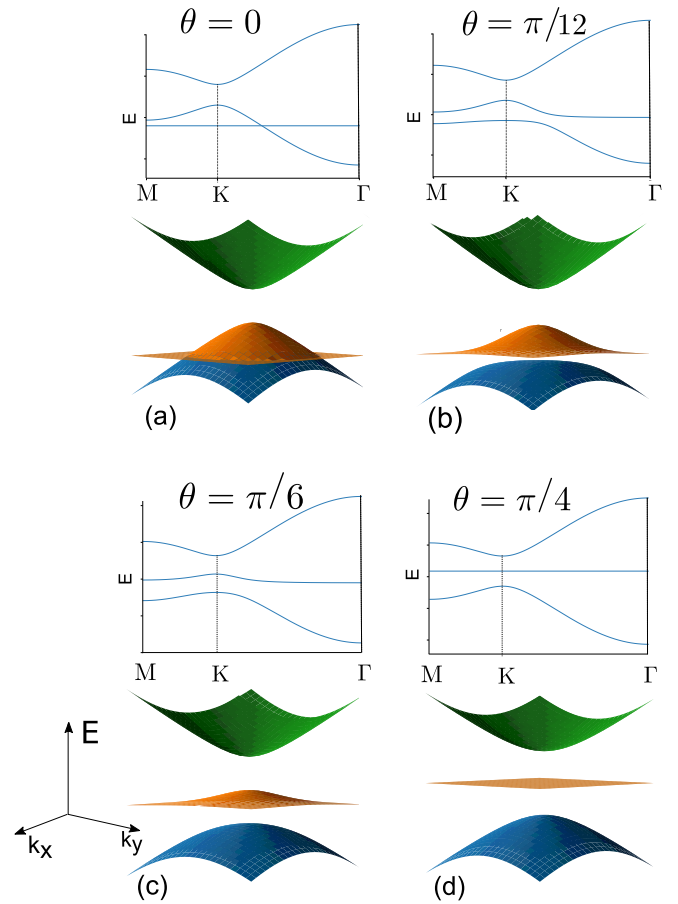

FIG. 4. Energy spectrum of Dirac fermions in the α-T_3 lattice for different values of θ when the symmetry-breaking term $\hat{U} = \hat{U}_2$ is used in Eq. (4). The full first Brillouin zone is shown at the top and below the energy spectrum around the K point for (a) $\theta = 0$ (graphenelike case), (b) $\theta = \pi/12$, (c) $\theta = \pi/6$, and (d) $\theta = \pi/4$ (dice case).

the eigenenergies

$$E_0 = \Delta, \quad E = \pm\sqrt{\Delta^2 + \hbar^2 v_F^2 k^2}. \tag{6}$$

Correspondingly, the wave functions in this case are given by

$$|\psi_0\rangle = \begin{pmatrix} \cos\theta e^{i\phi_k} \\ 0 \\ \sin\theta e^{-i\phi_k} \end{pmatrix}, \quad |\psi_\pm\rangle = \begin{pmatrix} \alpha\cos\theta e^{-i\phi_k} \\ \gamma \\ \alpha\sin\theta e^{i\phi_k} \end{pmatrix}, \tag{7}$$

where $\alpha = \sqrt{E + \Delta}$ and $\gamma = \sqrt{E - \Delta}$.

Similar sublattice symmetry-breaking systems have been discussed suggesting that such a mass potential term is attainable by depositing graphene on specific substrates, such as SiC [61,62] and h-BN [63]. In Eq. (6) we find the presence of a gap 2Δ opening in the energy spectrum. This results in massive Dirac fermions with an effective mass defined as $m = \Delta/v_F^2$. Since Eq. (6) does not depend on the parameter θ, the energy spectrum remains the same for all α-T_3 lattices, as shown in Fig. 3. Moreover, as long as the equivalence between the sites A and C is maintained, the flatband is shifted and touches only the bottom of the conduction band. Notice that
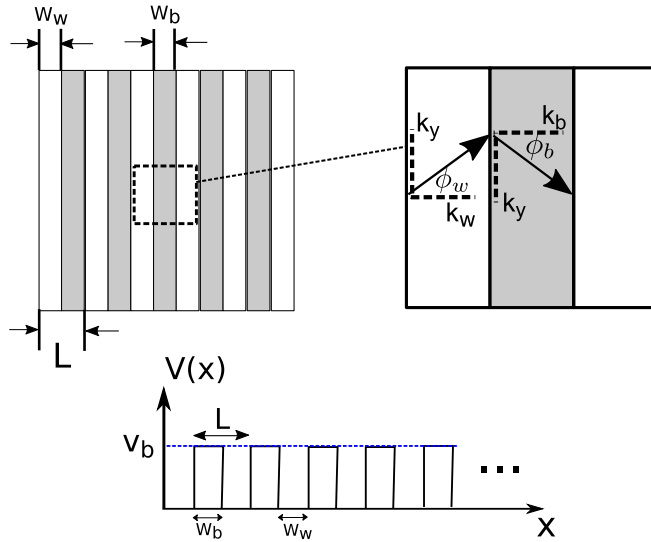
FIG. 5. Schematic representation of the superlattice potential in the *x*-*y* plane. Dark regions denote the barrier region with height $V(x) = V_b$ and the white region represents the well with zero potential. The angles ϕ_w and ϕ_b in the inset, respectively, denote the angles of the carriers in the wells and barriers regions. The profiles of the 1D periodic potential are given by the figure at the bottom.

now the bottom of the conduction band and the top of the valence band are quadratic in $\vec{k}$.

On the other hand, the term $\hat{U}_2$ defined in Eq. (5) has been used to describe the effect of a pseudomagnetic field [58,59], and the dispersion relations for this case are obtained from a solution of the nonlinear equation,

$$E(\Delta^2 - E^2) + k^2(\Delta \cos 2\theta + E) = 0, \qquad (8)$$

and the eigenstate for the conduction and valence bands is given by

$$|\psi\rangle = \begin{pmatrix} \alpha' \cos\theta e^{i\phi_k} \\ \gamma' \\ \beta \sin\theta e^{-i\phi_k} \end{pmatrix}, \qquad (9)$$

with $\alpha' = \sqrt{1 + 2\Delta/(E - \Delta)}$, $\gamma' = \sqrt{1 + \Delta\cos(2\theta)/E}$, and $\beta = \sqrt{1 - 2\Delta/(E + \Delta)}$.

Unlike the previous case, there is no longer equivalence between the site C and the other sites of the crystal structure, which means that small deviations of the coupling parameter α result in different eigenenergies as depicted in Fig. 4. In this case, the flatband is dispersionless only when $\theta = \pi/4$ (dice lattice) and is located in the center of the energy gap [59,60], as shown in Fig. 4(a).

III. SUPERLATTICE

In this paper, we investigate how fermions in α-T_3 lattices are affected by a one-dimensional periodic electrostatic potential. We investigate one-dimensional potentials with a periodicity much larger than the interatomic distance, i.e., $L/a_0 \ll 1$. We consider an infinite number of barriers periodically spaced with unit cell length $L = W_w + W_b$, with W_w (W_b) the width of the well (barrier), as illustrated in Fig. 5. The general Hamiltonian, taking into account the presence of

symmetry-breaking terms, is now given by [36,42,45]

$$\hat{H} = \hat{H}_{\text{kin}} + V(x)\hat{I} + \Delta\hat{U}_i, \qquad (10)$$

with $\hat{H}_{\text{kin}}$ given by Eq. (1), $V(x) = V_b$ the periodic potential, and $\Delta\hat{U}_i$ represents the symmetry-breaking term, which can be translated into a mass term. Due to translation invariance in the y direction, the wave functions have the form $\Psi_j(x, y) = \Psi_j(x)e^{ik_y y}$, with the label $j = w$ or $j = b$ used to denote the region of well (barrier), and $\Psi_j(x)$ is given by

$$\psi_j(x) = \frac{A}{\sqrt{2}} \begin{pmatrix} \alpha_j \cos\theta e^{i\phi_j} \\ \gamma_j \\ \beta_j \sin\theta e^{-i\phi_j} \end{pmatrix} e^{ik_j x}$$

$$+ \frac{B}{\sqrt{2}} \begin{pmatrix} -\alpha_j \cos\theta e^{-i\phi_j} \\ \gamma_j \\ -\beta_j \sin\theta e^{i\phi_j} \end{pmatrix} e^{-ik_j x}. \qquad (11)$$

The angles $\phi_w = \tan^{-1}(k_y/k_w)$ and $\phi_b = \tan^{-1}(k_y/k_b)$ are the angles associated with the direction of the momentum of the electron in the well and barrier regions, respectively, as depicted in the inset of Fig. 5, and both in addition to the terms α_j, γ_j, and β_j are obtained from the eigenstates equation using the Hamiltonian Eq. (10).

Moreover, the constants A, B, C, D are determined by requesting continuity of the wave functions. Writing the wave functions given by Eq. (11) in the general form $\Psi(x) = (\psi_A(x), \psi_B(x), \psi_C(x))$ and by integrating the eigenvalue equation $\hat{H}\Psi = E\Psi$ over a small interval $x = [-\epsilon, \epsilon]$ and allowing the interval to approach zero, we obtain the following matching conditions for the wave function on either side of the superlattice:

$$\psi_B(-\epsilon) = \psi_B(\epsilon) \qquad (12a)$$

and

$$\cos\theta\psi_A(-\epsilon) + \sin\theta\psi_C(-\epsilon) = \cos\theta\psi_A(\epsilon) + \sin\theta\psi_C(\epsilon). \qquad (12b)$$

These matching conditions are different from those of the two limiting cases in the α-T_3 model, i.e., graphenelike ($\alpha = 0$) and dice lattice ($\alpha = \pi/4$) [13,45]. For graphene, which has pseudospin-1/2, the matching conditions simply require the continuity of each two-component of the wave function. For the dice lattice, which has integer pseudospin, the matching condition takes into account a sum of the first and last component of the three components of the wave function, as indicated in Eq. (12) by setting $\cos\theta = \sin\theta = 1/\sqrt{2}$. Applying the matching conditions given by Eq. (12) into Eq. (11), we obtain the transfer matrix for the α-T_3 superlattice,

$$T = \Omega_{k_w}(L)\Omega_{k_w}^{-1}(W_b)\Omega_{k_b}(W_b)\Omega_{k_b}^{-1}(0), \qquad (13)$$

where

$$\Omega_{k_j}(x) = \begin{pmatrix} \gamma_j e^{ik_j x} & \gamma_j e^{-ik_j x} \\ \lambda_j e^{ik_w x} & -\lambda_j^* e^{-ik_w x} \end{pmatrix}, \qquad (14)$$

with

$$\lambda_j = \cos^2\theta e^{i\phi_j} + \sin^2\theta e^{-i\phi_j}. \qquad (15)$$

Inserting Eq. (14) into Eq. (13), we get

$$
T = \frac{1}{a_b a_w}
\begin{pmatrix}
c_+ \lambda_b^\dagger + c_- \lambda_b & \gamma_b(c_+ - c_-) \\
d_+ \lambda_b^\dagger + d_- \lambda_b & \gamma_b(d_+ - d_-)
\end{pmatrix},
\qquad (16)
$$

where

$$
a_j = \gamma_j(\lambda_j^* + \lambda_j), \qquad\qquad (17a)
$$

$$
c_+ = e^{ik_b W_b} \gamma_w (\gamma_b b_1 + \lambda_b b_2),
$$
$$
c_- = e^{-ik_b W_b} \gamma_w (\gamma_b b_1 - \lambda_b^* b_2), \qquad (17b)
$$

$$
d_+ = e^{ik_b W_b}(\gamma_b \lambda_w \lambda_w^* b_2 + \gamma_w \lambda_b b_3),
$$
$$
d_- = e^{-ik_b W_b}(\gamma_b \lambda_w \lambda_w^* b_2 - \gamma_w \lambda_b^* b_3), \qquad (17c)
$$

with $b_1 = \lambda_w^* e^{ik_w W_w} + \lambda_w e^{-ik_w W_w}$, $b_2 = e^{ik_w W_w} - e^{-ik_w W_w}$, and $b_3 = \lambda_w e^{ik_w W_w} + \lambda_w^* e^{-ik_w W_w}$.

According to Bloch's theorem and requiring $\det[T] = 1$, the electronic dispersion at any incident angle is given by $2\cos(K_x L) = \mathrm{Tr}(T)$, where $K_x = 2\pi n/L$ expresses the periodicity of the superlattice structure. This results in the following nonlinear equation for the dispersion relation:

$$
\cos(K_x L) = \cos(k_b W_b)\cos(k_w W_w)
$$
$$
- G_U \sin(k_b W_b)\sin(k_w W_w), \qquad (18)
$$

where G_U differs by the presence or absence of the symmetry-breaking term. It is denoted by G_0 for the gapless case, and G_1 and G_2 when $\hat{U}_1$ and $\hat{U}_2$ are taken into account, respectively. As we will demonstrate further on, since the dispersion relation given in Eq. (18) depends on the symmetry between

the atomic sites of the crystal structure, the inclusion of small deviations between them leads to large changes in the energy spectra and the band gap.

The allowed states for the superlattice are obtained when $-1 \leqslant \cos(K_x L) \leqslant 1$ in Eq. (18), which corresponds to the energy spectra for this system in the k_y plane. In addition, we can derive the density of states (DOS) represented by $D(E)$ and given by

$$
D(E) = \sum_{n,k_y} \delta(E - E_{n,k_y}), \qquad (19)
$$

and expressed in units of $D_0 = L/\hbar v_F$, which corresponds to the amount of states per unit area, and L is the period of the superlattice.

IV. PRISTINE SYSTEM

To start, we consider the pristine system corresponding to $\hat{U}_i = 0$ in Eq. (10). The solution of $\hat{H}\Psi_j = E\Psi_j$ in this case leads to $\alpha_j = \gamma_j = \beta_j = 1$ in the wave functions given by Eq. (11). Moreover, from the secular equation $\det(\hat{H} - E) = 0$ we obtain, respectively, the wave vectors in the x-direction in the well and barrier regions,

$$
k_w = \sqrt{\left(\frac{E}{\hbar v_F}\right)^2 - k_y^2}, \quad k_b = \sqrt{\left(\frac{E - V_b}{\hbar v_F}\right)^2 - k_y^2}, \quad (20)
$$

with $\hbar v_F = 3a_0 t/2$.

From the transfer matrix in Eq. (16) we find the dispersion relation given by Eq. (18) with $G_U = G_0$, where

$$
G_0 = \frac{1}{k_w k_b}\left[\frac{E(E - V_b)}{\hbar^2 v_F^2} + \frac{[E^2 + (E - V_b)^2]k_y^2[\cos^2(2\theta) - 1]}{2E(E - V_b)} - k_y^2 \cos^2(2\theta) \right]. \qquad (21)
$$

An electrostatic superlattice is capable of multiplying the number of Dirac points [21]. These are points in reciprocal space where the valence and conduction bands touch each other and around which the energy spectrum is linear. Therefore, it is interesting to calculate how the α-T_3 lattice Dirac point is affected by the superlattice potential.

To determine the location of the Dirac points for the symmetric case $W_b = W_w = W$, we take $K_x = 0$ and $k_b = k_w$ in Eq. (18). Inserting this latter condition into Eq. (20), we have $E = V_b/2$. Thus, Eq. (18) becomes

$$
1 = \cos^2(k_b W) + \sin^2(k_b W)
$$
$$
\times \left[\frac{V_0^2/4\hbar^2 v_F^2 + 2k_y^2 \cos^2(2\theta) - k_y^2}{V_0^2/4\hbar^2 v_F^2 - k_y^2} \right]. \qquad (22)
$$

This equation has solutions when the term between brackets is equal to 1, or $\sin^2(k_b W) = 1$. The first possibility is obtained for $k_y = 0$ and corresponds to the main Dirac point at $k_y = 0$. The second possibility leads to $k_b W = n\pi$ with n being a positive integer. This last possibility determines the position

of the extra Dirac points in k_y space from Eq. (20),

$$
k_y = \sqrt{\frac{V_b^2}{4\hbar^2 v_F^2} - \left(\frac{n\pi}{W}\right)^2}. \qquad (23)
$$

Note from Eq. (22) that for the symmetric case, the condition to determine the position of Dirac points is regardless of the parameter θ. Note that when $\theta = 0$, Eq. (22) reduces to

$$
1 = \cos^2(k_b W) + \sin^2(k_b W)
$$
$$
\times \left[(V_b^2/4\hbar^2 v_F^2 + k_y^2)/(V_b^2/4\hbar^2 v_F^2 - k_y^2) \right], \qquad (24)
$$

which is consistent with the equation that determines the Dirac points for graphene [21]. As discussed above, there is no real solution for Eq. (24) unless $k_y = 0$, which represents the usual Dirac point, or $k_b W = n\pi$ [18,21,22].

On the other hand, when we set $\theta = \pi/4$, Eq. (22) leads to

$$
\cos^2(k_b W) + \sin^2(k_b W) = 1. \qquad (25)
$$

Unlike the graphenelike case, Eq. (22) has many solutions and the condition for allowed states in the dispersion relation of Eq. (18) is always satisfied for arbitrary k_y.

In Figs. 6(a)–6(d) we show the electronic band structures at $K_x L = 0$ for some values of the parameter θ assuming
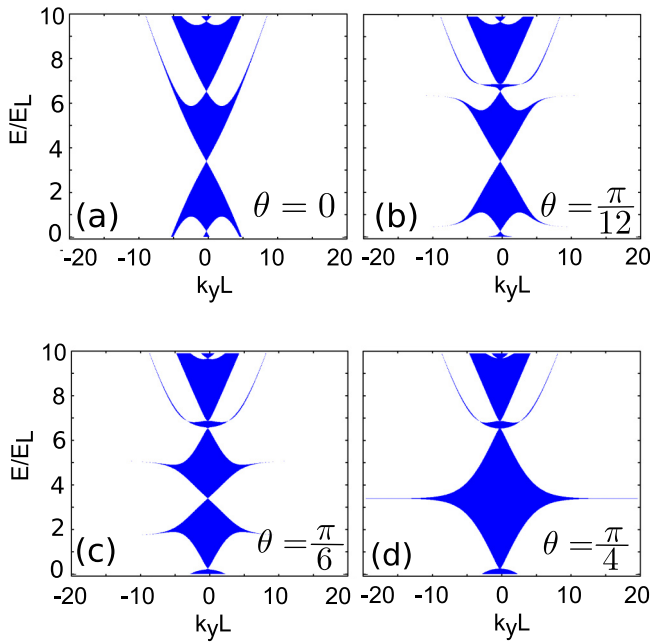
FIG. 6. Electronic band structures at $K_xL = 0$ for (a) $\theta = 0$ (graphenelike case), (b) $\theta = \pi/12$, (c) $\theta = \pi/6$, (d) $\theta = \pi/4$ (dice case) with $V_b = 7E_L$, $W_w = W_b = L/2$, where $L/a_0 = 1200$, and $E_L = \hbar v_F/L$.

$W_w = W_b = L/2$ and $V_b = 7E_L$, where $E_L = \hbar v_F/L$ and $L/a_0 = 1200$. As discussed above, one Dirac point appears at $E = V_b/2$ and $k_yL = 0$ for $0 \leqslant \theta < \pi/4$ as shown in Figs. 6(a)–6(c), moreover the upper and lower bands gradually becomes closer as the structure reaches $\theta = \pi/4$ (dice lattice), when the Dirac point disappears and all states at $E = 3.5E_L$ are allowed regardless of the values of k_yL, as shown in Fig. 6(d).

The dependence on the parameter θ observed in the energy spectra can be better understood from the density of states (DOS) shown in Fig. 7 for the same parameters as in Fig. 6.
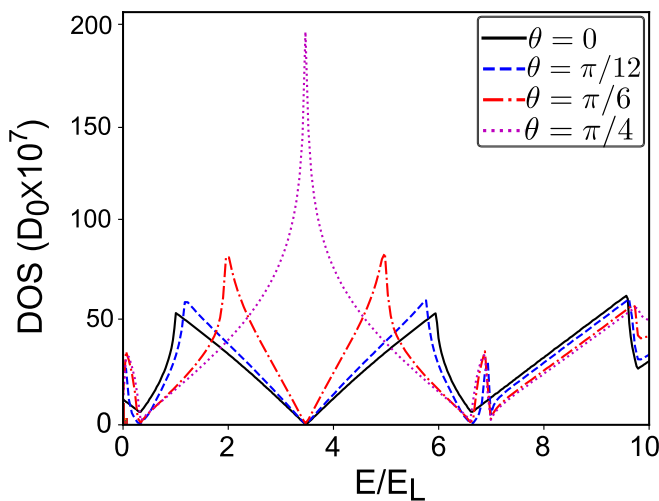
FIG. 7. Density of states for $\theta = 0$ (black solid curve), $\theta = \pi/12$ (blue dashed curve), $\theta = \pi/6$ (red dash-dotted curve), and $\theta = \pi/4$ (magenta dotted curve) for the same parameters as in Fig. 6.
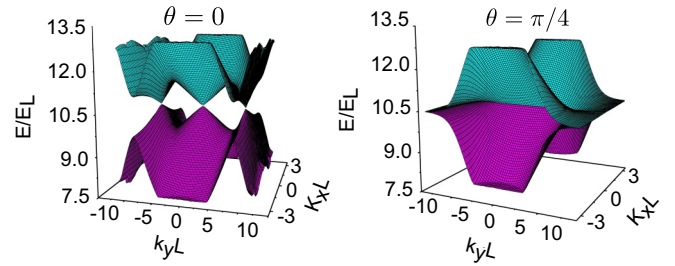

FIG. 8. Valence and conduction bands of the spectrum of a superlattice considering $\theta = 0$ (graphenelike), and $\theta = \pi/4$ (dice) with $V_b = 21E_L$, $W_w = W_b = L/2$, where $L/a_0 = 1200$, and $E_L = \hbar v_F/L$.

For the dice case, depicted by the magenta dotted curve, we notice the presence of a pronounced peak, which agrees with Eq. (25) representing the manifestation of the flatband and, therefore, an enhancement of the number of states.

In Fig. 8 the spectrum resulting from Eq. (18) using Eq. (21) for equal barrier and well width is plotted taking $L/a_0 = 1200$ and $V_b = 21E_L$ for $\theta = 0$ and $\theta = \pi/4$. We observe for the honeycomb case, i.e., $\theta = 0$, the appearance of extra Dirac points localized to the left and to the right of the main one at the energy corresponding to $V_b = 10.5E_L$ for $K_xL = 0$. However, at this same point for the dice case, the Dirac points disappear giving rise to a flatband. This can be observed more clearly in Fig. 9, where we show the superlattice spectrum along k_yL for $K_xL = 0$ for different values of θ. We notice that as θ increases, the spacing between the upper and lower bands around the Dirac points decreases. Moreover, the group velocity along the k_yL direction around the main and the extra Dirac points denoted in Fig. 9 by the labels I and II is shown in Fig. 10. Notice that the slope of the dispersion relation around these points is strongly reduced as compared to the value v_F when no superlattice is imposed.
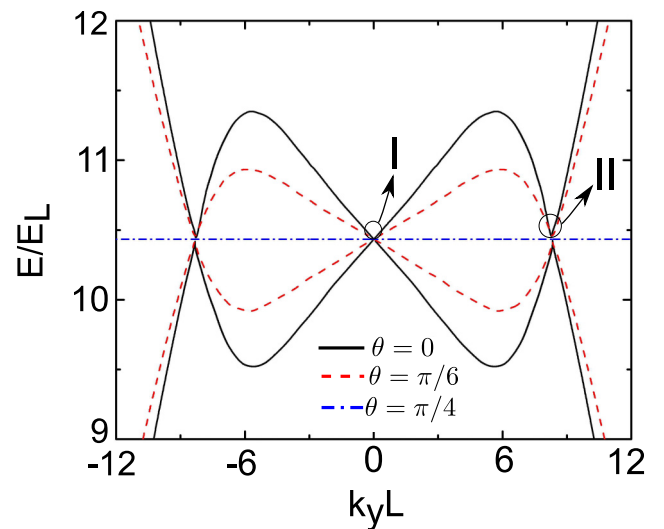

FIG. 9. Electronic band structures for $K_xL = 0$ with $\theta = 0$ (black solid curve), $\theta = \pi/6$ (red dashed curve), and $\theta = \pi/4$ (blue dot-dashed curve) for $K_xL = 0$ with $V_b = 21E_L$, $W_w = W_b = L/2$, where $L/a_0 = 1200$, and $E_L = \hbar v_F/L$.
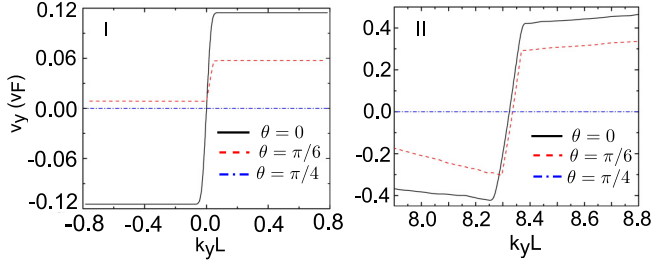
FIG. 10. Group velocity along the k_y direction around the main Dirac point (I), and around the extra Dirac point (II) indicated in Fig. 9.

This result is similar to the collimation effect observed in graphene as new extra Dirac points are to arise when the height of the potential V_b increases, as discussed in Ref. [21]. But now, the collimation effect results from changing the coupling constant θ.

V. INTRODUCTION OF GAPS IN THE SUPERLATTICE ENERGY SPECTRUM

Using the transfer-matrix formalism from Sec. III, we analyze the appearance and morphing in α-T_3 superlattices when including deviations in the atomic equivalence of the three sublattices and by adding the terms $\hat{U}_1$ or $\hat{U}_2$.

A. Case $\hat{U} = \hat{U}_1$

Assuming $\hat{U} = \hat{U}_1$ in Eq. (10), we obtain the wave functions expressed in Eq. (11) in the well ($j = w$) and barrier ($j = b$) with $\alpha_w = \beta_w = \sqrt{E + \Delta}$, $\alpha_b = \beta_b = \sqrt{E - V_b + \Delta}$, $\gamma_w = \sqrt{E - \Delta}$, and $\gamma_b = \sqrt{E - V_b - \Delta}$.

The wave vectors in the x-direction in the well and barrier regions are

$$k_w = \sqrt{\frac{E^2 - \Delta^2}{\hbar^2 v_F^2} - k_y^2}, \quad (26a)$$

$$k_b = \sqrt{\frac{(E - V_b)^2 - \Delta^2}{\hbar^2 v_F^2} - k_y^2}. \quad (26b)$$

From the transfer-matrix method we get the dispersion relation in Eq. (18) with $G_U = G_1$,

$$G_1 = -\frac{1}{2}\left[\left(\frac{\eta_{w_1}}{\eta_{b_1}} + \frac{\eta_{b_1}}{\eta_{w_1}}\right) + \cos^2(2\theta)\left(\frac{k_y^2}{k_b^2}\frac{\eta_{b_1}}{\eta_{w_1}} + \frac{k_y^2}{k_w^2}\frac{\eta_{w_1}}{\eta_{b_1}}\right) - 2\frac{k_y^2}{k_w k_b}\cos^2(2\theta)\right], \quad (27)$$

with $\eta_{w_1} = k_w \hbar v_F/(E - \Delta)$ and $\eta_{b_1} = k_b \hbar v_F/(E - V_b - \Delta)$.

To analyze the effects on the energy spectrum, and to investigate how the Dirac points are affected due to the presence of this symmetry-breaking term, we consider $W_b = W_W = W$, and $k_w W = -k_b W$ in Eq. (18) at the energy $E = V_b/2$, where, for the gapless case, the Dirac points are found. When we take into account these considerations and we assume $\theta = 0$, the dispersion relation becomes

$$\cos(K_x L) = \cos^2(k_b W) + \sin^2(k_b W) \times \left[\frac{(V_b^2/4 + \Delta^2)/\hbar^2 v_F^2 + k_y^2}{(V_b^2/4 - \Delta^2)/\hbar^2 v_F^2 - k_y^2}\right], \quad (28)$$

which has no real solution regardless of the value of k_y, indicating the presence of a band gap in the energy spectrum. This result can be extended to other cases where $\cos 2\theta \neq 0$ in Eq. (27).

Assuming the particular case $\theta = \pi/4$, we get

$$\cos(K_x L) = \cos^2(k_b W) + \sin^2(k_b W) \times \left[\frac{(V_b^2/4 + \Delta^2)/\hbar^2 v_F^2 - k_y^2[(V_b^2/4 + \Delta^2)/(V_b^2/4 - \Delta^2)]}{(V_b^2/4 - \Delta^2)/\hbar^2 v_F^2 - k_y^2}\right], \quad (29)$$

which has a real solution for two touching points $k_y = \pm\sqrt{V_b^2/4 - \Delta^2}/\hbar v_F$. Unlike the dice case in the absence of a mass term discussed in Sec. III, the energy-allowed states in the presence of a symmetry-breaking term are no longer independent of k_y at $E = V_b/2$.

This becomes more clear when we calculate the electronic band structure for some particular values of the parameter θ, the effective-mass term $\Delta = 0.1 V_b$, $V_b = 7E_L$, and $L/a_0 = 1200$. The results are depicted in Fig. 11, where $E_L = \hbar v_F/L$. As discussed from Eqs. (28) and (29), we can observe the presence of a band gap in the energy spectra at $E = V_b/2$, or, in terms of the unit E_L, $E \approx 3.5E_L$, except for $\theta = \pi/4$, where the band gap is closed at the touching points $k_y = \pm\sqrt{V_b^2/4 - \Delta^2}/\hbar v_F$, but we observe the formation of another band gap at energy $E \approx 5E_L$. Moreover, the minibands present in the energy spectra for intermediate values of θ are no longer symmetric around the band gap, as shown in Figs. 11(b) and 11(c). The band-gap morphing and its de-

pendence on θ can be observed when we analyze the density of states (DOS) of those systems shown in Fig. 12. The appearance of asymmetric minibands, and the band-gap shifting observed in Fig. 11(d), becomes clearly apparent. In addition, unlike the graphenelike case, when we assume $\theta \neq 0$ a new allowed energy state arises that appears as a new peak localized in the energy range $7E_L$–$8E_L$ as observed in Fig. 12.

On the other hand, when we take a large value for the mass term $\Delta = 0.4 V_b$ maintaining the other parameters used in Fig. 11, beyond the increased gap, we find that the minibands change drastically. When $\theta \neq 0$, the energy spectra exhibit significant modifications in a large range of energy, as shown in Figs. 13(b)–13(d), where it is possible to see the appearance of new minibands inside the band-gap region, unlike the graphenelike case. The appearance of new allowed states inside the region where for the graphenelike case there is only a band gap is clearly seen from the density of states, as shown in Fig. 14. In addition, the position of the touching points
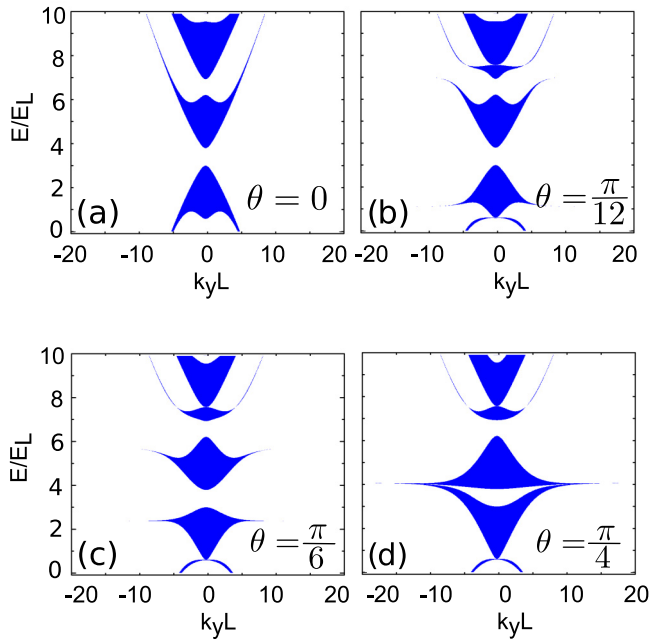
FIG. 11. Electronic band structures at $K_xL = 0$ for (a) $\theta = 0$ (graphenelike case), (b) $\theta = \pi/12$, (c) $\theta = \pi/6$, (d) $\theta = \pi/4$ (dice case) with $V_b = 7E_L$, $W_w = W_b = L/2$, $\Delta = 0.1V_b$, and $\hat{U} = \hat{U}_1$, where $L/a_0 = 1200$, and $E_L = \hbar v_F/L$ in all cases.

FIG. 13. Electronic band structures at $K_xL = 0$ for (a) $\theta = 0$ (graphenelike case), (b) $\theta = \pi/12$, (c) $\theta = \pi/6$, (d) $\theta = \pi/4$ (dice case) with $V_b = 7E_L$, $W_w = W_b = L/2$, $\Delta = 0.4V_b$ for $\hat{U} = \hat{U}_1$, where $L/a_0 = 1200$, and $E_L = \hbar v_F/L$ in all cases.

given by $k_y = \pm\sqrt{V_b^2/4 - \Delta^2}/\hbar v_F$ depends on the mass term value, and these points are shifted, as shown in Fig. 13(d). From Fig. 14 we observe that there is a prominent peak when the dice case is considered similar to Fig. 12 but localized at different energy, which results from the increase of the mass term Δ. Moreover, it is evident that there are more allowed states in the energy range $2E_L$–$5E_L$ for $\theta \neq 0$. In Fig. 15 we show the dispersion relation obtained from Eqs. (21) and (27) assuming equal barrier and well widths, $L/a_0 = 1200$, $V_b = 21E_L$, and $\Delta = 0.4V_b$ for $\theta = 0$ and $\theta = \pi/4$. Unlike

the gapless case, for $\theta = 0$ the main Dirac point at $k_yL = 0$ is no longer observed, although the extra Dirac points on both sides remain. Similarly, for the dice case, the upper and lower minibands touch each other at two points $k_yL \neq 0$, as in Figs. 11(d) and 13(d).

Moreover, when we assume the superlattice spectrum along the k_yL direction for $K_xL = 0$ in Fig. 15, we find that the dispersion gradually changes around the point $k_yL = 0$, becoming flat for $\theta = \pi/4$, as shown in Fig. 16. In addition,
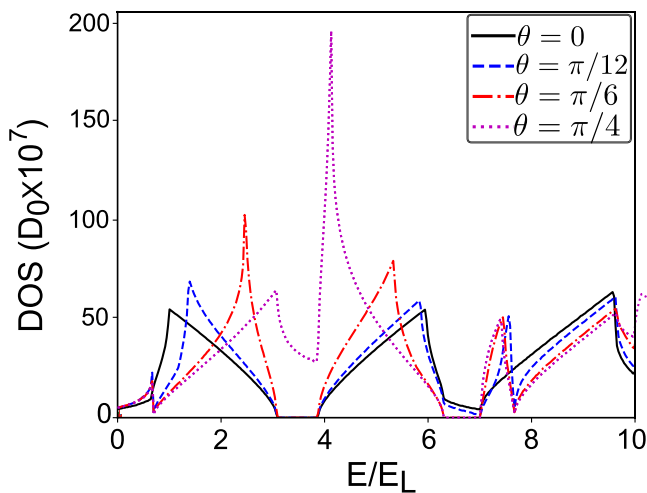

FIG. 12. Density of states for $\theta = 0$ (black solid curve), $\theta = \pi/12$ (blue dashed curve), $\theta = \pi/6$ (red dash-dotted curve), and $\theta = \pi/4$ (magenta dotted curve) for the same parameters as in Fig. 11.
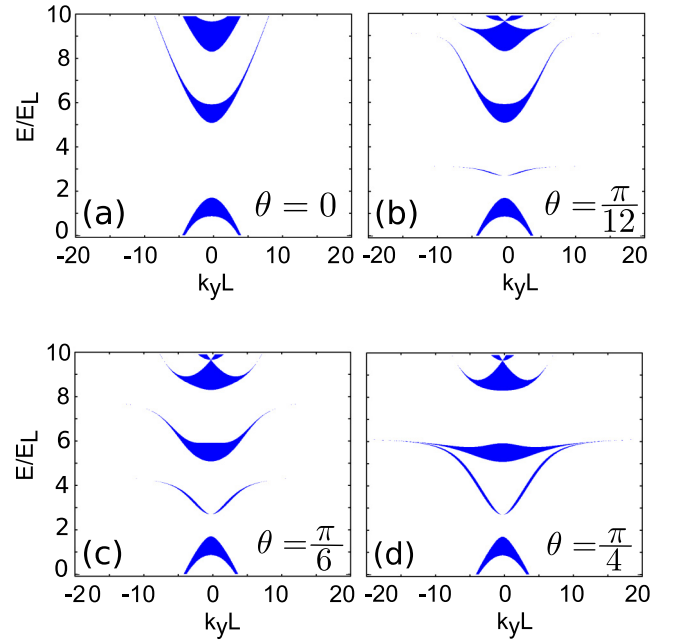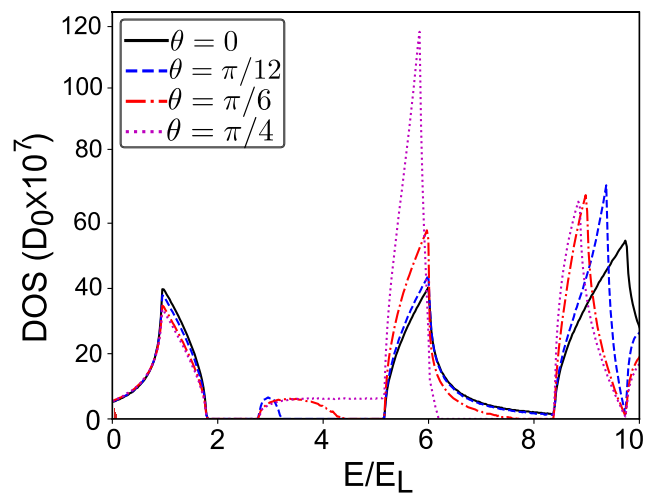

FIG. 14. Density of states for $\theta = 0$ (black solid curve), $\theta = \pi/12$ (blue dashed curve), $\theta = \pi/6$ (red dash-dotted curve), and $\theta = \pi/4$ (magenta dotted curve) for the same parameters as in Fig. 13.
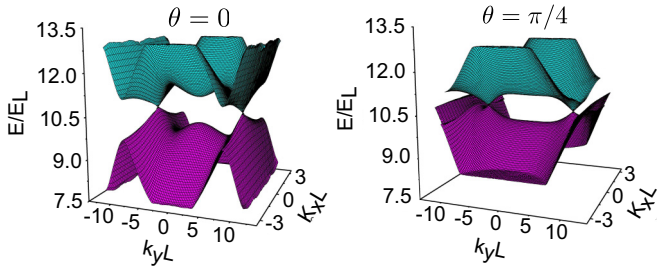
FIG. 15. Valence and conduction bands of the spectrum of a superlattice considering $\theta = 0$ (graphenelike), and $\theta = \pi/4$ (dice) with $V_b = 21E_L$, $W_w = W_b = L/2$, $\hat{U} = \hat{U}_1$, and $\Delta = 0.4V_b$, where $L/a_0 = 1200$, and $E_L = \hbar v_F/L$.

around the touching points the slope of the dispersion decreases as θ increases.

B. Case $\hat{U} = \hat{U}_2$

For the other symmetry-breaking term denoted by $\hat{U} = \hat{U}_2$ in Eq. (10), we have $\alpha_w = \sqrt{1 + 2\Delta/(E - \Delta)}$, $\alpha_b = \sqrt{1 + 2\Delta/(E - V_b - \Delta)}$, $\gamma_w = \sqrt{1 + \Delta\cos(2\theta)/E}$, $\gamma_b = \sqrt{1 + \Delta\cos(2\theta)/(E - V_b)}$, $\beta_w = \sqrt{1 - 2\Delta/(E + \Delta)}$, and $\beta_b = \sqrt{1 - 2\Delta/(E - V_b + \Delta)}$. Consequently, the wave functions k_w and k_b are given by

$$k_w = \sqrt{\frac{(E^2 - \Delta^2)E}{(\hbar^2 v_F^2)(E + \Delta\cos 2\theta)} - k_y^2}, \tag{30a}$$

$$k_b = \sqrt{\frac{[(E - V_b)^2 - \Delta^2](E - V_b)}{(\hbar^2 v_F^2)(E - V_b + \Delta\cos 2\theta)} - k_y^2}. \tag{30b}$$
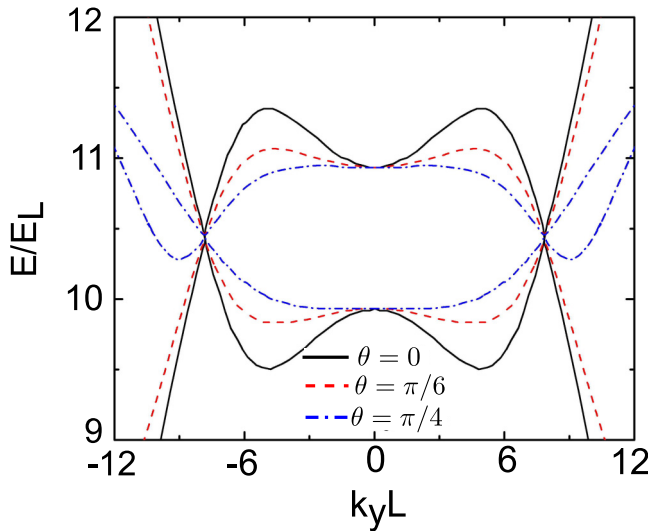

FIG. 16. Electronic band structures at $K_xL = 0$ for $\theta = 0$ (black solid curve), $\theta = \pi/6$ (red dashed curve), and $\theta = \pi/4$ (blue dot-dashed curve) with $V_b = 21E_L$, $W_w = W_b = L/2$, $\Delta = 0.4V_b$, where $L/a_0 = 1200$, and $E_L = \hbar v_F/L$.
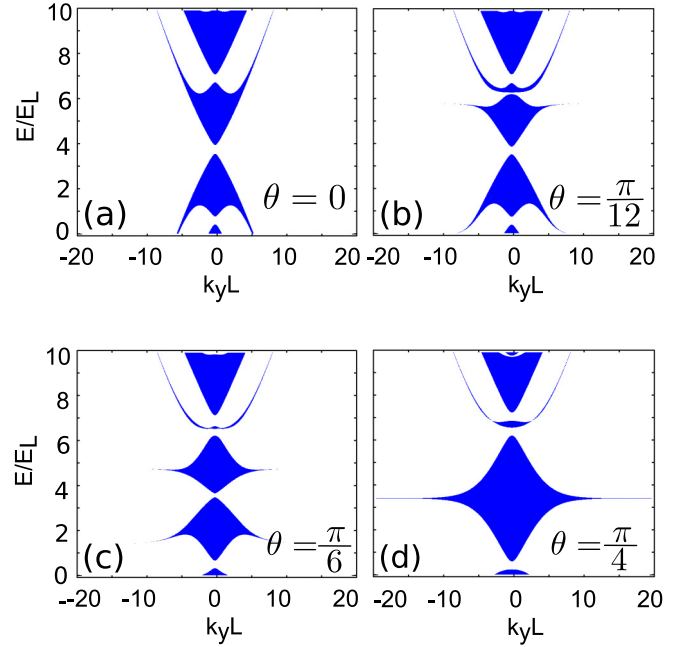

FIG. 17. Electronic band structures at $K_xL = 0$ for (a) $\theta = 0$ (graphenelike case), (b) $\theta = \pi/12$, (c) $\theta = \pi/6$, (d) $\theta = \pi/4$ (dice case) with $V_b = 7E_L$, $W_w = W_b = L/2$, $\Delta = 0.1V_b$ when $\hat{U} = \hat{U}_2$, where $L/a_0 = 1200$, and $E_L = \hbar v_F/L$ in all cases.

For this case, we have

$$G_2 = -\frac{1}{2}\left[\left(\frac{\eta_{w_2}}{\eta_{b_2}} + \frac{\eta_{b_2}}{\eta_{w_2}}\right) + \left(\frac{k_y^2\eta_{b_2}}{k_b^2\eta_{w_2}}\frac{[(E - V_b)\cos 2\theta + \Delta]^2}{(E - V_b + \Delta\cos 2\theta)^2}\right.\right.$$
$$\left.+ \frac{k_y^2\eta_{w_2}}{k_w^2\eta_{b_2}}\frac{(E\cos 2\theta + \Delta)^2}{(E + \Delta\cos 2\theta)^2}\right)$$
$$\left.- \frac{2k_y^2}{k_wk_b}\frac{[(E - V_b)\cos 2\theta + \Delta](E\cos 2\theta + \Delta)}{(E - V_b + \Delta\cos 2\theta)(E + \Delta\cos 2\theta)}\right], \tag{31}$$

and

$$\eta_{w_2} = \frac{k_w}{(E^2 - \Delta^2)(E + \Delta\cos 2\theta)}, \tag{32a}$$

$$\eta_{b_2} = \frac{k_b}{[(E - V_b)^2 - \Delta^2][(E - V_b) + \Delta\cos 2\theta]}. \tag{32b}$$

From Eq. (10) assuming $\Delta = 0.1V_b$ for $\hat{U} = \hat{U}_2$, and the same values of L and V_b as in Fig. 6, we get the energy spectra shown in Fig. 17 for different values of θ. Similar to the case $\hat{U} = \hat{U}_1$, we observe the presence of a band gap for all values of $\theta \neq \pi/4$ around $E = V_b/2$, i.e., $E = 3.5E_L$, and the minibands tend to reach each other around this energy as θ increases until the band gap is completely closed for the dice case, as shown in Fig. 17(d). Like the gapless case, all energy states when $\theta = \pi/4$ are allowed regardless of the k_y value, which results in a prominent peak in the density of states depicted in Fig. 18. This result can be expected when we assume the condition $W_b = W_w = W$, $E = V_b/2$, and $\theta = \pi/4$ in the dispersion relation for this case. Under these conditions, the dispersion relation for the dice lattice reduces to the same one for the gapless case represented in Eq. (25).
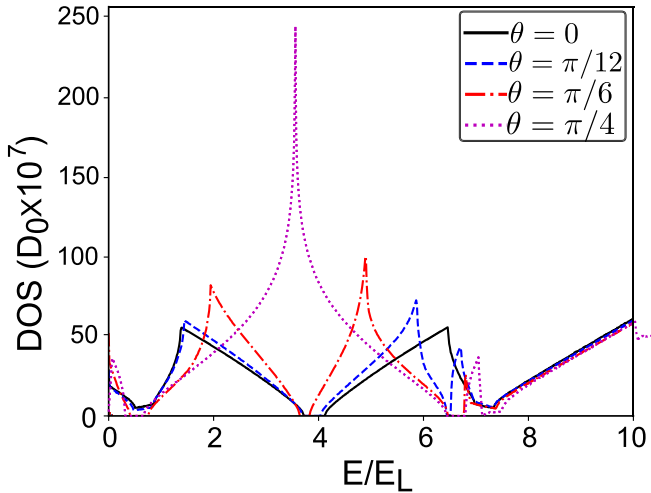
FIG. 18. Density of states for $\theta = 0$ (black solid curve), $\theta = \pi/12$ (blue dashed curve), $\theta = \pi/6$ (red dash-dotted curve), and $\theta = \pi/4$ (magenta dotted curve) for the same parameters as in Fig. 17.

FIG. 20. Density of states for $\theta = 0$ (black solid curve), $\theta = \pi/12$ (blue dashed curve), $\theta = \pi/6$ (red dash-dotted curve), and $\theta = \pi/4$ (magenta dotted curve) for the same parameters as in Fig. 19.

Moreover, comparing the band-gap width observed in Fig. 17 to the one in Fig. 11, the band gap is reduced and shifted up, as observed in Fig. 18.

Similar to the previous gapped case, if we consider a larger value of the mass term $\Delta = 0.4V_b$, the band gap is increased and other allowed states appear inside them when intermediate values of θ are considered, as shown in Fig. 19. However, the allowed state for arbitrary values of k_y at $E = V_b/2$ for the dice lattice is preserved, and a peak in the density of states is observed for $\theta = \pi/4$, as shown in Fig. 20, since this condition is independent of the value of the effective mass.
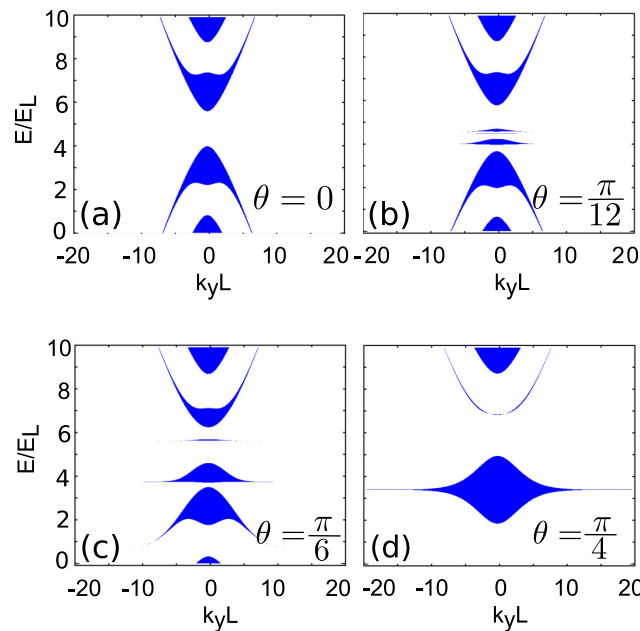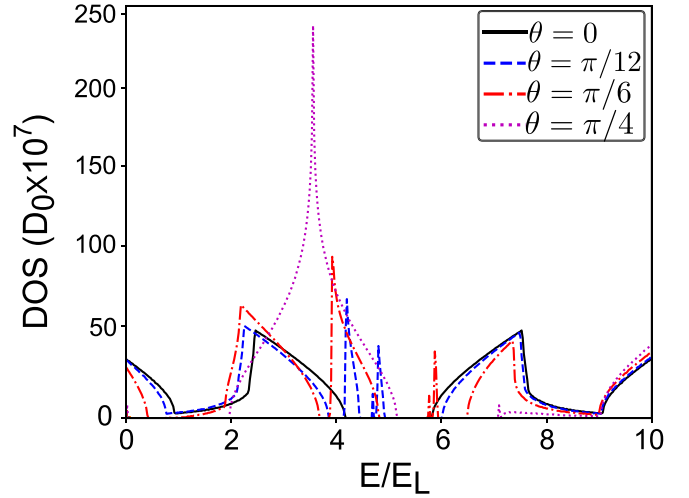
The spectrum obtained from Eqs. (18) and (31) considering equal barrier and well widths, $L/a_0 = 1200$, $V_b = 21E_L$, and $\Delta = 0.4V_b$ for $\theta = 0$ and $\theta = \pi/4$, is shown in Fig. 21. Similar to a previous gapped case, for $\theta = 0$ the upper and lower minibands touch each other in two points, and at $k_yL = 0$ there is a gap. However, as discussed above, the energy where the touching points are localized is no longer at $E = V_b/2$. On the other hand, for the dice lattice the spectrum is completely flat at $k_yL = 0$ and $E = V_b/2$, similar to Fig. 8.

In Fig. 22 we show the superlattice spectrum considering $K_xL = 0$ along the k_yL direction for some values of θ. Notice that the energy where the touching points are localized depends on θ. Moreover, like the gapless case, as $\theta \to \pi/4$ the dispersion becomes flat and shifted to lower values of energy.

VI. CONCLUSIONS

We investigated the energy spectrum and the density of states (DOS) of α-T_3 lattices for different values of interlattice hopping parameter $\theta = \tan^{-1} \alpha$ in the presence of a 1D superlattice. We consider both the case of equivalence between the three sublattices, and how the band gap is affected by small deviations of this equivalence in the limit $\Delta \ll t$ by

FIG. 19. Electronic band structures at $K_xL = 0$ for (a) $\theta = 0$ (graphenelike case), (b) $\theta = \pi/12$, (c) $\theta = \pi/6$, (d) $\theta = \pi/4$ (dice lattice) with $V_b = 7E_L$, $W_w = W_b = L/2$, $\Delta = 0.4V_b$ when $\hat{U} = \hat{U}_2$, where $L = 1200$, and $E_L = \hbar v_F/L$ in all cases.
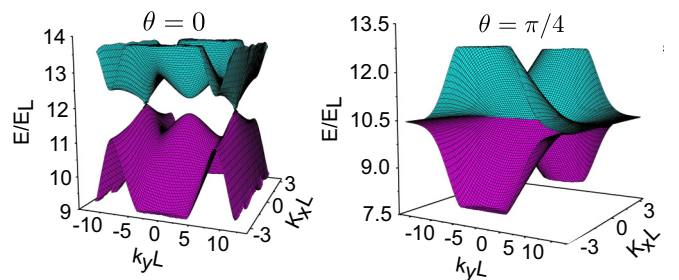

FIG. 21. Valence and conduction bands of the spectrum of a superlattice considering $\theta = 0$ (graphenelike), and $\theta = \pi/4$ (dice) with $V_b = 21E_L$, $W_w = W_b = L/2$, $\hat{U} = \hat{U}_2$, and $\Delta = 0.4V_b$, where $L/a_0 = 1200$, and $E_L = \hbar v_F/L$.
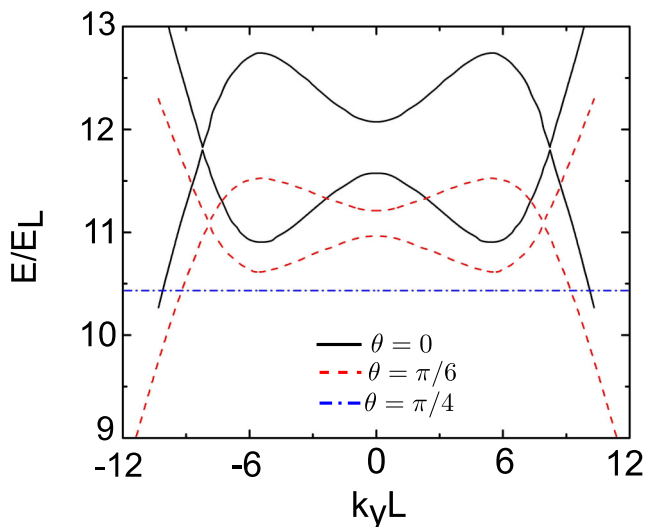
FIG. 22. Electronic band structures at $K_x L = 0$ for $\theta = 0$ (black solid curve), $\theta = \pi/6$ (red dashed curve), and $\theta = \pi/4$ (blue dot-dashed curve) with $V_b = 21 E_L$, $W_w = W_b = L/2$, $\Delta = 0.4 V_b$, where $L/a_0 = 1200$, and $E_L = \hbar v_F / L$.

considering two cases of symmetry-breaking terms denoted by $\hat{U}_1$ and $\hat{U}_2$.

For the pristine system, when no symmetry-breaking term is present, we found the condition for the appearance of Dirac points that depends on the cosine function of the parameter θ, indicating that the energy level where they are located remains the same for all cases when $\cos(2\theta) \neq 1$. When $\theta = \pi/4$, all energies are allowed for arbitrary k_y. Moreover, the minibands for intermediate values of θ tend to close around the energy level where Dirac points are localized. In addition, when we considered higher values of the potential, we observed extra Dirac points localized on the right and on the left of the main one positioned at $k_y = 0$ for all values of $\theta \neq \pi/4$.

When we introduce symmetry-breaking terms into the system, we observed the appearance of a band gap, whose creation depends on the deviation of the equivalence between the three sublattices. When we considered the case

$\hat{U}_1 = \text{diag}(1, -1, 1)$, a band gap appears at energy $E = V_b/2$. However for the dice case, around this energy, there is no longer a band gap, and the minibands touch at two points. This result can be observed both in the energy spectra and in their corresponding DOS.

In addition, the minibands for larger values of the mass term were shifted up, which is a consequence of the fact that the sites A and C remain equivalent, leading to twofold degeneracy of the energy spectra, as in the case when there is no periodic potential present. Moreover, for larger values of the potential, the main Dirac point for all θ values is no longer present; only the extra ones appear and are localized at the energy $E = V_b/2$.

When $\hat{U}_2 = \text{diag}(1, 0, -1)$, the dispersion relation, and consequently the energy spectrum, is strongly altered. For the dice case, we found that the condition for the allowance of the energy states at $E = V_b/2$ is always satisfied regardless of k_y, similar to the gapless case. However, a band gap is still present but is now localized at another energy. In addition, we noticed that the band gap is smaller than the one observed when $\hat{U}_1$. Moreover, for larger values of the effective mass, new energy states were observed inside the band gap as confirmed from the density of states. In addition, for higher values of the potential considering $\theta \neq \pi/4$ only the extra Dirac points are observed, as for the previous gapped case, but now the energy value where they are localized depends on the hopping parameter.

The theoretical formalism and results obtained in this work are useful for a better understanding of the band-gap behavior of α-T_3 lattices, and consequently they demonstrate that these materials are versatile for purposes of band-gap engineering in 2D materials, since the band gap is tunable by changing the interlattice hopping parameter and the symmetry.

ACKNOWLEDGMENTS

[1] K. S. Novoselov, A. K. Geim, S. V. Morozov, D. Jiang, Y. Zhang, S. V. Dubonos, I. V. Grigorieva, and A. A. Firsov, Electric field effect in atomically thin carbon films, Science **306**, 666 (2004).

[2] S. V. Morozov, K. S. Novoselov, M. I. Katsnelson, F. Schedin, D. C. Elias, J. A. Jaszczak, and A. K. Geim, Giant Intrinsic Carrier Mobilities in Graphene and Its Bilayer, Phys. Rev. Lett. **100**, 016602 (2008).

[3] M. I. Katsnelson, K. S. Novoselov, and A. K. Geim, Chiral tunnelling and the Klein paradox in graphene, Nat. Phys. **2**, 620 (2006).

[4] E. B. Sonin, Effect of Klein tunneling on conductance and shot noise in ballistic graphene, Phys. Rev. B **79**, 195438 (2009).

[5] H. Liu, A. T. Neal, Z. Zhu, Z. Luo, X. Xu, D. Tománe, and P. D. Ye, Phosphorene: An unexplored 2D semiconductor with a high hole mobility, ACS Nano **8**, 4033 (2014).

[6] C.-C. Liu, H. Jiang, and Y. Yao, Low-energy effective Hamiltonian involving spin-orbit coupling in silicene and two-dimensional germanium and tin, Phys. Rev. B **84**, 195430 (2011).

[7] M. E. Dávila, L. Xian, S. Cahangirov, A. Rubio, and G. Le Lay, Germanene: a novel two-dimensional germanium allotrope akin to graphene and silicene, New J. Phys. **16**, 095002 (2014).

[8] D. P. DiVincenzo and E. J. Mele, Self-consistent effective-mass theory for intralayer screening in graphite intercalation compounds, Phys. Rev. B **29**, 1685 (1984).

[9] N. M. R. Peres, Scattering in one-dimensional heterostructures described by the Dirac equation, J. Phys.: Condens. Matter **21**, 095501 (2009).

[10] N. Stander, B. Huard, and D. Goldhaber-Gordon, Evidence for Klein Tunneling in Graphene p-n Junctions, Phys. Rev. Lett. **102**, 026807 (2009).

[11] A. Young and P. Kim, Quantum interference and Klein tunnelling in graphene heterojunctions, Nat. Phys. **5**, 222 (2009).

[12] B. Huard, J. A. Sulpizio, N. Stander, K. Todd, B. Yang, and D. Goldhaber-Gordon, Transport Measurements Across a Tunable Potential Barrier in Graphene, Phys. Rev. Lett. **98**, 236803 (2007).

[13] P. E. Allain and J. N. Fuchs, Klein tunneling in graphene: Optics with massless electrons, Eur. Phys. J. B **83**, 301 (2011).

[14] R. Tsu, *Superlattice to Nanoelectronics* (Elsevier, Oxford, 2005).

[15] C. Bai and X. Zhang, Klein paradox and resonant tunneling in a graphene superlattice, Phys. Rev. B **76**, 075430 (2007).

[16] C. H. Park, L. Yang, Y. W. Son, M. L. Cohen, and S. G. Louie, Anisotropic behaviours of massless Dirac fermions in graphene under periodic potentials, Nat. Phys. **4**, 213 (2008).

[17] M. Barbier, F. M. Peeters, P. Vasilopoulos, and J. Milton Pereira, Jr., Dirac and Klein-Gordon particles in one-dimensional periodic potentials, Phys. Rev. B **77**, 115446 (2008).

[18] L. G. Wang and S.-Y. Zhu, Electronic band gaps and transport properties in graphene superlattices with one-dimensional periodic potentials of square barriers, Phys. Rev. B **81**, 205444 (2010).

[19] J. Sun, H. A. Fertig, and L. Brey, Effective Magnetic Fields in Graphene Superlattices, Phys. Rev. Lett. **105**, 156801 (2010).

[20] L. Z. Tan, C.-H. Park, and S. G. Louie, Graphene Dirac fermions in one-dimensional inhomogeneous field profiles: Transforming magnetic to electric field, Phys. Rev. B **81**, 195426 (2010).

[21] M. Barbier, P. Vasilopoulos, and F. M. Peeters, Extra Dirac points in the energy spectrum for superlattices on single-layer graphene, Phys. Rev. B **81**, 075438 (2010).

[22] L. Brey and H. A. Fertig, Emerging Zero Modes for Graphene in a Periodic Potential, Phys. Rev. Lett. **103**, 046809 (2009).

[23] C.-H. Park, Y.-W. Son, L. Yang, M. L. Cohen, and S. G. Louie, Landau Levels and Quantum Hall Effect in Graphene Superlattices, Phys. Rev. Lett. **103**, 046808 (2009).

[24] M. Barbier, P. Vasilopoulos, and F. M. Peeters, Single-layer and bilayer graphene superlattices: Collimation, additional Dirac points and Dirac lines, Philos. Trans. R. Soc. A **368**, 5499 (2010).

[25] C. H. Park, Y. W. Son, L. Yang, M. L. Cohen, and S. G. Louie, Electron beam supercollimation in graphene superlattices, Nano Lett. **8**, 2920 (2008).

[26] Y. Li, S. Dietrich, C. Forsythe, T. Taniguchi, K. Watanabe, P. Moon, and C. R. Dean, Anisotropic band flattening in graphene with one-dimensional superlattices, Nat. Nanotechnol. **16**, 525 (2021).

[27] S. Borisenko, Q. Gibson, D. Evtushinsky, V. Zabolotnyy, B. Büchner, and R. J. Cava, Experimental Realization of a Three-Dimensional Dirac Semimetal, Phys. Rev. Lett. **113**, 027603 (2014).

[28] M. Slot, T. Gardenier, P. Jacobse, G. C. P. van Miert, S. N. Kempkes, S. J. M. Zevenhuizen, C. M. Smith, D. Vanmaekelbergh, and I. Swart, Experimental realization and characterization of an electronic Lieb lattice, Nat. Phys. **13**, 672 (2017).

[29] Z. Li, J. Zhuang, L. Wang, H. Feng, Q. Gao, X. Xu, W. Hao, X. Wang, C. Zhang, K. Wu, S. X. Dou, L. Chen, Z. Hu, and

Y. Du, Realization of flat band with possible nontrivial topology in electronic Kagome lattice, Science Adv. **4**, aau4511 (2018).

[30] Z. K. Liu, B. Zhou, Y. Zhang, Z. J. Wang, H. M. Weng, D. Prabhakaran, S.-K. Mo, Z. X. Shen, Z. Fang, X. Dai, Z. Hussain, and Y. L. Chen, Discovery of a three-dimensional topological Dirac semimetal, Na_3Bi, Science **343**, 864 (2014).

[31] B. Dóra, J. Kailasvuori, and R. Moessner, Lattice generalization of the Dirac equation to general spin and the role of the flat band, Phys. Rev. B **84**, 195422 (2011).

[32] A. Raoux, M. Morigi, J.-N. Fuchs, F. Piéchon, and G. Montambaux, From Dia- to Paramagnetic Orbital Susceptibility of Massless Fermions, Phys. Rev. Lett. **112**, 026402 (2014).

[33] B. Sutherland, Localization of electronic wave functions due to local topology, Phys. Rev. B **34**, 5208 (1986).

[34] E. H. Lieb, Two Theorems on the Hubbard Model, Phys. Rev. Lett. **62**, 1201 (1989).

[35] J. D. Malcolm and E. J. Nicol, Magneto-optics of general pseudospins two-dimensional Dirac-Weyl fermions, Phys. Rev. B **90**, 035405 (2014).

[36] Z. Lan, N. Goldman, A. Bermudez, W. Lu, and P. Öhberg, Dirac-Weyl fermions with arbitrary spin in two-dimensional optical superlattices, Phys. Rev. B **84**, 165115 (2011).

[37] L. Wang and D.-X. Yao, Coexistence of spin-1 fermion and Dirac fermion on the triangular kagome lattice, Phys. Rev. B **98**, 161403(R) (2018).

[38] E. Illes, Properties of the $\alpha - T_3$ Model, Ph.D. thesis, University of Guelph, Canada, 2017.

[39] A. Iurov, G. Gumbs, and D. Huang, Peculiar electronic states, symmetries, and Berry phases in irradiated $\alpha - T_3$ materials, Phys. Rev. B **99**, 205135 (2019).

[40] Y. Xie, Y. Tan, and A. W. Ghosh, Spintronic signatures of Klein tunneling in topological insulators, Phys. Rev. B **96**, 205151 (2017).

[41] Y. Xu and G. Jin, Omnidirectional transmission and reflection of pseudospin-1 Dirac fermions in a Lieb superlattice, Phys. Lett. A **378**, 3554 (2014).

[42] D. F. Urban, D. Bercioux, M. Wimmer, and W. Häusler, Barrier transmission of Dirac-like pseudospin-one particles, Phys. Rev. B **84**, 115136 (2011).

[43] C.-Y. Tan, C.-X. Yan, Y.-H. Zhao, H. Guo, and H.-R. Chang, Anisotropic longitudinal optical conductivities of tilted Dirac bands in $1T' - MoS_2$, Phys. Rev. B **103**, 125425 (2021).

[44] N. Weekes, A. Iurov, L. Zhemchuzhna, G. Gumbs, and D. Huang, Generalized WKB theory for electron tunneling in gapped $\alpha - T_3$ lattices, Phys. Rev. B **103**, 165429 (2021).

[45] E. Illes and E. J. Nicol, Klein tunneling in the $\alpha - T_3$ model, Phys. Rev. B **95**, 235432 (2017).

[46] S. Peotta and P. Törmä, Superfluidity in topologically nontrivial flat bands, Nat. Commun. **6**, 8944 (2015).

[47] A. Julku, S. Peotta, T. I. Vanhala, D.-H. Kim, and P. Törmä, Geometric Origin of Superfluidity in the Lieb-Lattice Flat Band, Phys. Rev. Lett. **117**, 045303 (2016).

[48] L. Mandhour and F. Bouhadida, Klein tunneling in deformed $\alpha - T_3$ lattice, arXiv:2004.10144.

[49] J. Y. Vaishnav and C. W. Clark, Observing Zitterbewegung with Ultracold Atoms, Phys. Rev. Lett. **100**, 153002 (2008).

[50] B. Dey and T. K. Ghosh, Floquet topological phase transition in the $\alpha - T_3$ lattice, Phys. Rev. B **99**, 205429 (2019).

[51] F. Wang and Y. Ran, Nearly flat band with Chern number $C = 2$ on the dice lattice, Phys. Rev. B **84**, 241103(R) (2011).

[52] D. Bercioux, D. F. Urban, H. Grabert, and W. Häusler, Massless dirac-weyl fermions in a T_3 optical lattice, Phys. Rev. A **80**, 063603 (2009).

[53] D. D. Edwall, J. S. Chen, J. Bajaj, and E. R. Gertner, MOCVD Hg1-xCdxTe/GaAs for IR detectors, Semicond. Sci. Technol. **5**, S221 (1990).

[54] Y. Betancur-Ocampo and V. Gupta, Perfect transmission of 3D massive Kane fermions in HgCdTe Veselago lenses, J. Phys.: Condens. Matter **30**, 035501 (2018).

[55] C. H. Yang, R. Wieser, and L. Wang, The effect of a variable coupling parameter on the tunneling properties from graphene to $\alpha - T_3$ model, J. Appl. Phys. **128**, 094301 (2020).

[56] R. Shen, L. B. Shao, B. Wang, and D. Y. Xing, Single Dirac cone with a flat band touching on line-centered-square optical lattices, Phys. Rev. B **81**, 041410(R) (2010).

[57] C. Xu, G. Wang, Z. Hang, J. Luo, C. T. Chan, and Y. Lai, Design of full-k-space flat bands in photonic crystals beyond the tight-binding picture, Sci. Rep. **5**, 18181 (2015).

[58] J. Romhányi, K. Penc, and R. Ganesh, Hall effect of triplons in a dimerized quantum magnet, Nat. Commun. **6**, 6805 (2015).

[59] E. V. Gorbar, V. P. Gusynin, and D. O. Oriekhov, Electron states for gapped pseudospin-1 fermions in the field of a charged impurity, Phys. Rev. B **99**, 155124 (2019).

[60] D. Green, L. Santos, and C. Chamon, Isolated flat bands and spin-1 conical bands in two-dimensional lattices, Phys. Rev. B **82**, 075104 (2010).

[61] S. Kim, J. Ihm, H. J. Choi, and Y.-W. Son, Origin of Anomalous Electronic Structures of Epitaxial Graphene on Silicon Carbide, Phys. Rev. Lett. **100**, 176802 (2008).

[62] M. S. Nevius, M. Conrad, F. Wang, A. Celis, M. N. Nair, A. Taleb-Ibrahimi, A. Tejeda, and E. H. Conrad, Semiconducting Graphene from Highly Ordered Substrate Interactions, Phys. Rev. Lett. **115**, 136802 (2015).

[63] S. Y. Zhou, G.-H. Gweon, A. V. Fedorov, P. N. First, W. A. de Heer, D.-H. Lee, F. Guinea, A. H. Castro Neto, and A. Lanzara, Substrate-induced bandgap opening in epitaxial graphene, Nat. Mater. **6**, 770 (2007).